JOURNAL OF GUIDANCE, CONTROL, AND DYNAMICS
Vol. 30, No. 2, March–April 2007

Electromagnetic Formation Flight Dynamics Including Reaction Wheel Gyroscopic Stiffening Effects

Laila M. Elias,* Daniel W. Kwon,† Raymond J. Sedwick,‡ and David W. Miller§
Massachusetts Institute of Technology, Cambridge, Massachusetts 02139

DOI: 10.2514/1.18679

In this paper, we consider the equations of motion of a two-spacecraft formation flying array that uses electromagnets as relative position actuators. The relative positions of the spacecraft are controlled by the forces generated between the electromagnets on the two spacecraft, and the attitudes of the spacecraft are controlled using reaction wheels. The nonlinear equations of motion for this system are linearized about a nominal operating trajectory, taken to be a steady-state spin maneuver used for deep-space interferometric observation. The linearized equations are analyzed for stability and controllability. Although the open-loop system proves to be unstable, a controllability analysis indicates that the system is fully controllable with the given suite of actuators, and is therefore stabilizable. An optimal linear feedback controller is then designed, and the closed-loop dynamics are simulated. The simulations demonstrate that the closed-loop system is indeed stable, and that linear control is a very promising technique for electromagnetic formation flight systems, despite the nonlinearity of the dynamics.

I. Introduction

OPTICAL interferometry, the collecting of light through multiple apertures and the interference of that light to yield meaningful data, is a very promising technology for future space science. Like a traditional monolithic space telescope that performs better with a larger aperture, interferometers gain improved angular resolution with greater spacing between the apertures. For this reason, and because of the improved visibility outside of the Earth's atmosphere, space-based interferometry may allow us to see further into the universe than ever before. One architecture that has been proposed for implementing interferometry in deep space is placing separated apertures on formation flying spacecraft.

NASA's future Terrestrial Planet Finder (TPF) is a mission considering the use of separated-spacecraft interferometry. The use of thrusters to control the relative degrees of freedom raises several concerns for TPF, including a limited mission lifetime associated with the finite fuel supply, as well as optical and thermal contamination by the thruster plumes. A suggestion to avoid these problems is the use of electromagnets on the spacecraft to generate magnetic fields, whereby the interactions of the fields cause forces and torques to be applied to the spacecraft [1]. This is a contaminant-free and "rechargeable" (using solar arrays) solution.

In this paper, we consider a two-spacecraft electromagnetic formation flying (EMFF) array, where each spacecraft is equipped with three orthogonal electromagnets (EMs) and three orthogonal reaction wheels (RWs). We begin by describing the system and reviewing the nonlinear equations of motion. We then present the linearized dynamics of the system. The system will be linearized about a steady-state spin trajectory, which is useful for data collection in space interferometry applications such as TPF. Specifically, the two spacecraft will nominally follow a circular trajectory about the center point of the array, within a fixed plane of rotation. Further, the spacecraft will nominally rotate such that their attitudes remain fixed with respect to the center of the array. Hence one reaction wheel on each spacecraft, the one whose spin axis is aligned with the spin axis of the array, will store the angular momentum of the array, and thus will operate at much higher spin rates than the other reaction wheels. For this reason, we model the nonlinear dynamics of this reaction wheel on each spacecraft. The other two reaction wheel actuators are modeled simply as motor torques on the spacecraft. The linearized dynamics will be analyzed for stability and controllability. A linear controller will then be designed and implemented in closed-loop dynamic simulations.

Received 19 April 2006; accepted for publication 22 July 2006.

*Ph.D. Candidate, Department of Aeronautics and Astronautics; currently Senior Engineer, Guidance and Control Analysis Group, Jet Propulsion Laboratory, California Institute of Technology, M/S 198-326, Pasadena, CA 91109. Member AIAA.

†Graduate Research Assistant, Department of Aeronautics and Astronautics, Room 37-344a, Student Member AIAA.

‡Principal Research Scientist, Department of Aeronautics and Astronautics, Room 37-431, 77 Massachusetts Avenue. Senior Member AIAA.

§Professor, Department of Aeronautics and Astronautics; Director Space Systems Laboratory, Room 37-327. Senior Member AIAA.

II. System Description

A. Coordinate Frames

We first describe the geometry of the system being considered. In [2], Kane's method is used to derive the nonlinear equations of motion for a multispacecraft EMFF system. We consider here a simplified, two-spacecraft array. The two vehicles, denoted as spacecraft A and B, are depicted in Fig. 1. Also depicted in Fig. 1 are three different coordinate frames. First, the global Cartesian frame is defined as a triad of orthonormal unit vectors:

$$\hat{e}_G = \lfloor \hat{e}_x \quad \hat{e}_y \quad \hat{e}_z \rfloor^T \tag{1}$$

Similarly, local, body-fixed frames are defined on spacecraft A and B, respectively, as

$$\hat{e}_A = \lfloor \hat{a}_1 \quad \hat{a}_2 \quad \hat{a}_3 \rfloor^T, \qquad \hat{e}_B = \lfloor \hat{b}_1 \quad \hat{b}_2 \quad \hat{b}_3 \rfloor^T \tag{2}$$

Finally, a spherical, curvilinear frame is defined as:

$$\hat{e}_S = \lfloor \hat{e}_r \quad \hat{e}_\phi \quad \hat{e}_\psi \rfloor^T \tag{3}$$

As shown in Fig. 1, r is the distance from the origin of the global frame to spacecraft A, ψ is the angle between the position vector of spacecraft A ($\boldsymbol{r}_{AG}$) and the $\hat{e}_x$, $\hat{e}_y$ plane, and ϕ is the angle between $\hat{e}_x$ and the projection of $\boldsymbol{r}_{AG}$ onto the $\hat{e}_x$, $\hat{e}_y$ plane. Further, because $\hat{e}_S$ is a curvilinear frame, its unit vectors ($\hat{e}_r$, $\hat{e}_\phi$, $\hat{e}_\psi$) move with spacecraft A to form a local frame whose origin lies at the center of mass of spacecraft A. These unit vectors are not fixed to the body's attitude. As shown in Fig. 2, $\hat{e}_r$ always aligns with the position vector, $\boldsymbol{r}_{AG}$, of spacecraft A. Hence if spacecraft A lies on the surface of an imaginary sphere of radius r centered at the origin of the global

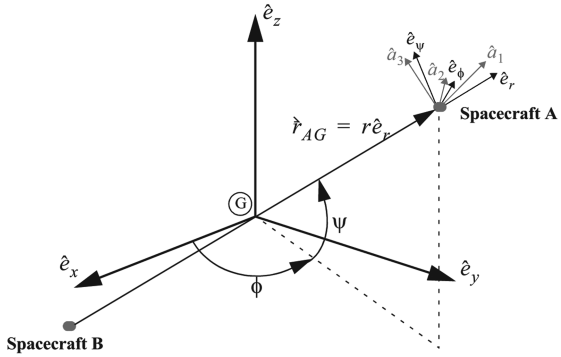

Fig. 1 Geometry of two-spacecraft EMFF array.

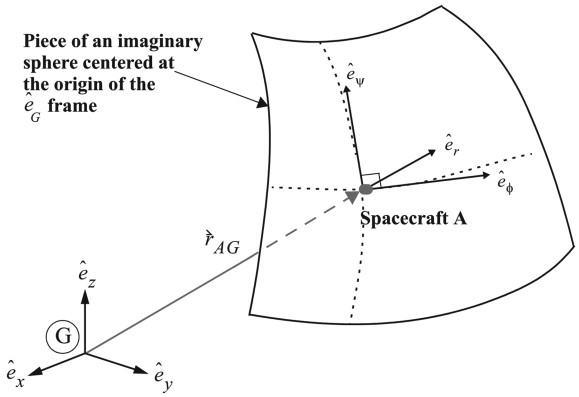

Fig. 2 Local curvilinear coordinate frame at spacecraft A.

frame, then $\hat{e}_r$ is perpendicular to the spherical surface, $\hat{e}_\phi$ is tangent to the spherical surface and parallel to the local line of constant latitude, and $\hat{e}_\psi$ is tangent to the spherical surface and parallel to the local line of constant longitude.

Figure 3 shows an additional coordinate frame, $\hat{e}_D$ that is body-fixed to RW-3, the reaction wheel on spacecraft A whose nonlinear dynamics will be modeled. The frame's origin is fixed at the RW-3 mass center, and the frame rotates with the wheel about its spin axis, $\hat{d}_3$, with respect to $\hat{e}_A$. $\hat{e}_D$ is composed of a triad of unit vectors:

$$\hat{e}_D = \lfloor \hat{d}_1 \quad \hat{d}_2 \quad \hat{d}_3 \rfloor^T \tag{4}$$

B. Degrees of Freedom

We now define the following degrees of freedom for spacecraft A:

1) r, ϕ, and ψ are curvilinear coordinates defining the position vector of spacecraft A, as depicted in Fig. 1. The position of spacecraft A may equivalently be expressed in Cartesian coordinates, x_{AG}, y_{AG}, and z_{AG}

2) α_3, α_2, and α_1 are the Euler angle rotations of spacecraft A about its body-fixed (principal) $\hat{a}_3$-, $\hat{a}_2$-, and $\hat{a}_1$-axes, respectively. The Euler angles are defined such that when they are zero, the $\hat{e}_A$ frame is aligned with $\hat{e}_G$.

3) δ_3 is the rotation angle of the RW on spacecraft A whose spin axis is aligned with $\hat{a}_3$. We refer to this RW as RW-3.

Before defining the degrees of freedom of spacecraft B, we first consider the nominal trajectory about which the equations of motion will be linearized. As described, the two-spacecraft array will nominally operate in a steady-state spin trajectory. The array will rotate in a circular trajectory within the global $\hat{e}_x$, $\hat{e}_y$ plane about the common center of the array. Further, spacecraft A and B will nominally rotate about their body-fixed $\hat{a}_3$- and $\hat{b}_3$-axes, respectively, to maintain a fixed attitude with respect to the center of the array. All other rotations of the spacecraft are nominally zero. Hence the position of spacecraft B is opposite that of spacecraft A

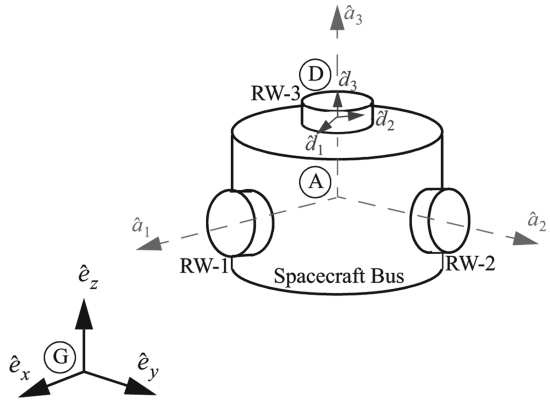

Fig. 3 Representative model of spacecraft A.

with respect to the global frame. Further, we make the following assumptions. First, we neglect the external loads on the spacecraft, because we will attempt to demonstrate closed-loop control of the linearized system without yet accounting for noise or external disturbances. An initial external disturbance will be modeled as a nonzero initial condition, and we will simulate the free response. Secondly, we treat spacecraft A and B as being identical in mass and geometric properties without any loss of generality, to further simplify the linearization and simulation of the equations of motion. Because of these assumptions, and because spacecraft B nominally lies opposite spacecraft A with respect to $\hat{e}_G$, the center of mass of the array will remain fixed in space, and will coincide with the origin of the global frame. Thus if the position of spacecraft A is defined by coordinates (r, ϕ, ψ), where $-\frac{\pi}{2} \le \psi \le \frac{\pi}{2}$, then the position of spacecraft B is defined by coordinates $(r, \phi + \pi, -\psi)$. Although the position coordinates of spacecraft B were treated as independent variables in the original dynamic derivation [2], we treat them here as dependent variables, or functions of the position of A.

The independent degrees of freedom of spacecraft B are then as follows:

1) β_3, β_2, and β_1 are the Euler angle rotations of spacecraft B about its body-fixed (principal) $\hat{b}_3$-, $\hat{b}_2$-, and $\hat{b}_1$-axes, respectively.

2) ε_3 is the rotation angle of RW-3 on spacecraft B about $\hat{b}_3$, the body-fixed axis on spacecraft B that is nominally aligned with $\hat{e}_z$.

C. Rotation Matrices

We now define three rotation matrices as functions of an arbitrary angle, θ:

$$R_1(\theta) \equiv \begin{bmatrix} 1 & 0 & 0 \\ 0 & c\theta & -s\theta \\ 0 & s\theta & c\theta \end{bmatrix}, \qquad R_2(\theta) \equiv \begin{bmatrix} c\theta & 0 & s\theta \\ 0 & 1 & 0 \\ -s\theta & 0 & c\theta \end{bmatrix},$$
$$R_3(\theta) \equiv \begin{bmatrix} c\theta & -s\theta & 0 \\ s\theta & c\theta & 0 \\ 0 & 0 & 1 \end{bmatrix} \tag{5}$$

where $c\theta$ and $s\theta$ denote $\cos(\theta)$ and $\sin(\theta)$, respectively. It is simple to see that these rotation matrices allow us to relate the Cartesian, body-fixed, and spherical coordinate frames as follows:

$$\hat{e}_G = R_3(\alpha_3)R_2(\alpha_2)R_1(\alpha_1)\hat{e}_A \tag{6}$$

$$\hat{e}_G = R_3(\beta_3)R_2(\beta_2)R_1(\beta_1)\hat{e}_B \tag{7}$$

$$\hat{e}_G = R_3(\phi)R_2(-\psi)\hat{e}_S \tag{8}$$

$$\hat{e}_A = R_3(\delta_3)\hat{e}_D \tag{9}$$

or conversely, because $R_i^{-1}(\theta) = R_i^T(\theta)$ for $i = 1, 2, 3$,

$$\hat{e}_A = R_1^T(\alpha_1)R_2^T(\alpha_2)R_3^T(\alpha_3)\hat{e}_G \tag{10}$$

$$\hat{e}_B = R_1^T(\beta_1)R_2^T(\beta_2)R_3^T(\beta_3)\hat{e}_G \tag{11}$$

$$\hat{e}_S = R_2^T(-\psi)R_3^T(\phi)\hat{e}_G = R_2(\psi)R_3^T(\phi)\hat{e}_G \tag{12}$$

$$\hat{e}_D = R_3^T(\delta_3)\hat{e}_A \tag{13}$$

Hence the vector components resolved on the various frames may also be related to one another using Eqs. (6–13). For example, the position vector, $\boldsymbol{r}_{AG}$, may be resolved on the global frame, $\hat{e}_G$, with components x_{AG}, y_{AG}, and z_{AG}. It may be equivalently resolved on the spherical frame, $\hat{e}_S$ with a component r to describe the distance from the origin, and the angles ϕ and ψ to define orientation of the spherical frame relative to the global frame. Hence $\boldsymbol{r}_{AG}$ may be expressed as

$$\boldsymbol{r}_{AG} = \lfloor\, x_{AG} \quad y_{AG} \quad z_{AG} \,\rfloor \hat{e}_G = \lfloor\, r \quad 0 \quad 0 \,\rfloor \hat{e}_S \tag{14}$$

where $\hat{e}_G$ and $\hat{e}_S$ are related by Eqs. (8) and (12). Substituting Eq. (12) for $\hat{e}_S$ into Eq. (14), we define the following relationships between the Cartesian and spherical coordinates of the position vector:

$$x_{AG} = r\cos\psi\cos\phi, \qquad y_{AG} = r\cos\psi\sin\phi, \qquad z_{AG} = r\sin\psi \tag{15}$$

Conversely, we find from geometry (and from the definitions of ϕ and ψ in Sec. II.A)

$$\begin{aligned} r &= \sqrt{x_{AG}^2 + y_{AG}^2 + z_{AG}^2}, \qquad \phi = \arctan\left(\frac{y_{AG}}{x_{AG}}\right), \\ \psi &= \arctan\left(\frac{z_{AG}}{\sqrt{x_{AG}^2 + y_{AG}^2}}\right) \qquad \left(-\frac{\pi}{2} \le \psi \le \frac{\pi}{2}\right) \end{aligned} \tag{16}$$

D. Angular Velocities

From the definitions of the Euler angles, it is simple to show that the angular velocities of the spacecraft and RW, respectively, may be defined as

$${}^G\boldsymbol{\omega}^A = \lfloor\, {}^G\omega_1^A \quad {}^G\omega_2^A \quad {}^G\omega_3^A \,\rfloor \hat{e}_A \tag{17}$$

$$\begin{aligned} {}^A\boldsymbol{\omega}^D &= \lfloor\, {}^A\omega_1^D \quad {}^A\omega_2^D \quad {}^A\omega_3^D \,\rfloor \hat{e}_D, \\ {}^G\boldsymbol{\omega}^D &= \lfloor\, {}^G\omega_1^D \quad {}^G\omega_2^D \quad {}^G\omega_3^D \,\rfloor \hat{e}_D \end{aligned} \tag{18}$$

where ${}^G\boldsymbol{\omega}^A$ is the angular velocity vector of spacecraft A with respect to the global frame, ${}^A\boldsymbol{\omega}^D$ is the angular velocity vector of the $\hat{e}_D$ frame on RW-3 with respect to the $\hat{e}_A$ frame on spacecraft A, and ${}^G\boldsymbol{\omega}^D = {}^A\boldsymbol{\omega}^D + {}^G\boldsymbol{\omega}^A$ is the angular velocity vector of the $\hat{e}_D$ frame on RW-3 with respect to the global frame. All of the relevant components are defined in Table 1.

E. Electromagnetic Force and Torques

Finally, we characterize the electromagnetic forces and torques between the spacecraft. On spacecraft A, the three perpendicular EMs are defined to align with the $\hat{a}_1$-, $\hat{a}_2$-, and $\hat{a}_3$-axes, respectively. On spacecraft B, they align with $\hat{b}_1$, $\hat{b}_2$, and $\hat{b}_3$, respectively. Assuming that the three electromagnets on each spacecraft are identical, we define the magnetic dipole moments on spacecraft A as

$$\boldsymbol{\mu}_{A_j} = \mu_{A_j}\hat{a}_j = n_A A_A i_{A_j}\hat{a}_j \qquad j = 1, 2, 3 \tag{19}$$

Table 1 Components of the angular velocity vectors in terms of Euler angles

Angular velocity vomponent	Definition (function of Euler angles)
${}^G\omega_1^A$	$-\dot{\alpha}_3 s\alpha_2 + \dot{\alpha}_1$
${}^G\omega_2^A$	$\dot{\alpha}_3 s\alpha_1 c\alpha_2 + \dot{\alpha}_2 c\alpha_1$
${}^G\omega_3^A$	$\dot{\alpha}_3 c\alpha_1 c\alpha_2 - \dot{\alpha}_2 s\alpha_1$
${}^A\omega_1^D$	0
${}^A\omega_2^D$	0
${}^A\omega_3^D$	$\dot{\delta}_3$
${}^G\omega_1^D$	${}^A\omega_1^D + c\delta_3\,{}^G\omega_1^A + s\delta_3\,{}^G\omega_2^A$
${}^G\omega_2^D$	${}^A\omega_2^D - s\delta_3\,{}^G\omega_1^A + c\delta_3\,{}^G\omega_2^A$
${}^G\omega_3^D$	${}^A\omega_3^D + {}^G\omega_3^A$

where n_A is the number of conductor layers (or "turns") for each coil on spacecraft A, A_A is the cross-sectional area for a single layer of the conductor used on spacecraft A, and i_{A_j} is the current running through the jth coil on spacecraft A. Analogous magnetic moments may be defined for the three coils on spacecraft B. If the resultant magnetic moment of spacecraft A is

$$\begin{aligned} \boldsymbol{\mu}_A &\equiv \boldsymbol{\mu}_{A_1} + \boldsymbol{\mu}_{A_2} + \boldsymbol{\mu}_{A_3} = n_A A_A \lfloor\, i_{A_1} \quad i_{A_2} \quad i_{A_3} \,\rfloor \hat{e}_A \\ &= n_A A_A \lfloor\, i_{A_1} \quad i_{A_2} \quad i_{A_3} \,\rfloor R_1^T(\alpha_1)R_2^T(\alpha_2)R_3^T(\alpha_3)\hat{e}_G \end{aligned} \tag{20}$$

and an analogous term may be expressed for spacecraft B, then the force and torque exerted on the EMs of spacecraft A by those of spacecraft B are, respectively [3],

$$\boldsymbol{F}_{AB} = \boldsymbol{\mu}_A \cdot \nabla \boldsymbol{B}_B|_A \tag{21}$$

$$\boldsymbol{T}_{AB} = \boldsymbol{\mu}_A \times \nabla \boldsymbol{B}_B|_A \tag{22}$$

where ∇ represents the gradient operator, B_B represents the spatially varying magnetic field due to $\boldsymbol{\mu}_B$, and $\cdot|_A$ indicates evaluation of the field at the location of spacecraft A.

The field due to $\boldsymbol{\mu}_B$ at an arbitrary position $\boldsymbol{\xi} = \xi\hat{e}_\xi$ relative to spacecraft B is

$$\boldsymbol{B}_B(\xi) = \frac{\mu_0}{4\pi\xi^3}[-\boldsymbol{\mu}_B + 3(\boldsymbol{\mu}_B \cdot \hat{e}_\xi)\hat{e}_\xi] \tag{23}$$

where $\mu_0 = 4\pi \times 10^{-7}$ T · m/A is the permeability constant. Assuming that $2r$ is the distance between spacecraft A and B, and $\hat{e}_r$ is the unit vector pointing from spacecraft B to spacecraft A, then the field due to $\boldsymbol{\mu}_B$ at the location of spacecraft A is

$$\boldsymbol{B}_B|_A = \frac{\mu_0}{4\pi(2r)^3}[-\boldsymbol{\mu}_B + 3(\boldsymbol{\mu}_B \cdot \hat{e}_r)\hat{e}_r] \tag{24}$$

Note that $\boldsymbol{B}_A|_B$, the field due to $\boldsymbol{\mu}_A$ at the location of spacecraft B, may be determined by simply replacing $\boldsymbol{\mu}_B$ with $\boldsymbol{\mu}_A$ in Eq. (21) and (22). Finally, evaluating Eqs. (21) and (22) yields

$$\begin{aligned} \boldsymbol{F}_{AB} = \frac{3\mu_0}{64\pi r^4}[&(\boldsymbol{\mu}_A \cdot \boldsymbol{\mu}_B)\hat{e}_r + (\boldsymbol{\mu}_A \cdot \hat{e}_r)\boldsymbol{\mu}_B + (\boldsymbol{\mu}_B \cdot \hat{e}_r)\boldsymbol{\mu}_A \\ &- 5(\boldsymbol{\mu}_A \cdot \hat{e}_r)(\boldsymbol{\mu}_B \cdot \hat{e}_r)\hat{e}_r] \end{aligned} \tag{25}$$

$$\boldsymbol{T}_{AB} = \boldsymbol{\mu}_A \times \frac{\mu_0}{4\pi(2r)^3}[-\boldsymbol{\mu}_B + 3(\boldsymbol{\mu}_B \cdot \hat{e}_r)\hat{e}_r] \tag{26}$$

III. Equations of Motion

A. Nonlinear Equations of Motion

In expressing the nonlinear equations of motion of the two-spacecraft array, we make one final simplifying assumption. We neglect the offset of the RW center of mass from the spacecraft center of mass without loss of generality. The term is not significant to the dynamics of the system, and neglecting it will simplify the eventual

linearization and simulation of the dynamics. With this assumption, the nonlinear equations of motion derived in [2] reduce to

$$(m_A + m_D)\ddot{\boldsymbol{r}}_{AG} = \boldsymbol{F}_{AB} \tag{27}$$

$$\begin{aligned}&{}^G\dot{\omega}_1^A I_1^A - {}^G\omega_2^{AG}\omega_3^A(I_2^A - I_3^A) + [\mathrm{c}\delta_3][{}^G\dot{\omega}_1^D I_1^D - {}^G\omega_2^{DG}\omega_3^D(I_2^D - I_3^D)]\\ &\quad - [\mathrm{s}\delta_3][{}^G\dot{\omega}_2^D I_2^D - {}^G\omega_3^{DG}\omega_1^D(I_3^D - I_1^D)] = T_{AB,1} - T_{Am_1}\end{aligned} \tag{28}$$

$$\begin{aligned}&{}^G\dot{\omega}_2^A I_2^A - {}^G\omega_3^{AG}\omega_1^A(I_3^A - I_1^A) + [\mathrm{s}\delta_3][{}^G\dot{\omega}_1^D I_1^D - {}^G\omega_2^{DG}\omega_3^D(I_2^D - I_3^D)]\\ &\quad + [\mathrm{c}\delta_3][{}^G\dot{\omega}_2^D I_2^D - {}^G\omega_3^{DG}\omega_1^D(I_3^D - I_1^D)] = T_{AB,2} - T_{Am_2}\end{aligned} \tag{29}$$

$${}^G\dot{\omega}_3^A I_3^A - {}^G\omega_1^{AG}\omega_2^A(I_1^A - I_2^A) = T_{AB,3} - T_{Am_3} \tag{30}$$

$${}^G\dot{\omega}_3^D I_3^D = T_{Am_3} \tag{31}$$

where m_A is the mass of spacecraft A, m_D is the mass of RW-3, I_i^A is the inertia of the spacecraft about the $\hat{a}_i$-axis ($i = 1, 2, 3$), I_i^D is the inertia of RW-3 about the $\hat{d}_i$-axis ($i = 1, 2, 3$), and $-T_{Am_i}$ is the RW motor torque applied to the spacecraft about the $\hat{a}_i$-axis. $\ddot{\boldsymbol{r}}_{AG}$ may be expressed by twice differentiating Eq. (14):

$$\begin{aligned}\ddot{\boldsymbol{r}}_{AG} &= \lfloor \ddot{x}_{AG} \;\; \ddot{y}_{AG} \;\; \ddot{z}_{AG} \rfloor \hat{e}_G = \lfloor \ddot{r} \;\; 0 \;\; 0 \rfloor \hat{e}_S + 2\lfloor \dot{r} \;\; 0 \;\; 0 \rfloor \dot{\hat{e}}_S\\ &\quad + \lfloor r \;\; 0 \;\; 0 \rfloor \ddot{\hat{e}}_S = \begin{Bmatrix} \ddot{r} - r\dot{\psi} - r\dot{\phi}^2\cos^2\psi \\ r\ddot{\phi}\cos\psi + 2\dot{r}\dot{\phi}\cos\psi - 2r\dot{\phi}\dot{\psi}\sin\psi \\ r\ddot{\psi} + 2\dot{r}\dot{\psi} + r\dot{\phi}^2\sin\psi\cos\psi \end{Bmatrix}^T \hat{e}_S\end{aligned} \tag{32}$$

and $\boldsymbol{F}_{AB}$ may be expressed as

$$\begin{aligned}\boldsymbol{F}_{AB} &= \lfloor F_{AB,x} \quad F_{AB,y} \quad F_{AB,z} \rfloor \hat{e}_G = \lfloor F_{AB,1} \quad F_{AB,2} \quad F_{AB,3} \rfloor \hat{e}_A\\ &= \lfloor F_{AB,r} \quad F_{AB,\phi} \quad F_{AB,\psi} \rfloor \hat{e}_S\end{aligned} \tag{33}$$

Recall that for the electromagnetic forces between two spacecraft to be calculated using Eq. (25), the magnetic moment vectors, $\boldsymbol{\mu}_A$ and $\boldsymbol{\mu}_B$, must first be transformed from components resolved on the spacecraft's body-fixed frame ($\hat{e}_A$ or $\hat{e}_B$) to components resolved on the global frame ($\hat{e}_G$) using Eq. (20). Further, Eqs. (27) and (32) require that the resulting force vector be transformed from components resolved on the global frame ($\hat{e}_G$) to components resolved on the curvilinear frame ($\hat{e}_S$) using Eq. (8):

$$\begin{aligned}\boldsymbol{F}_{AB} &= \lfloor F_{AB,x} \quad F_{AB,y} \quad F_{AB,z} \rfloor \hat{e}_G\\ &= \lfloor F_{AB,x} \quad F_{AB,y} \quad F_{AB,z} \rfloor R_3(\phi)R_2(-\psi)\hat{e}_S\end{aligned} \tag{34}$$

$$\begin{aligned}&\Rightarrow \lfloor F_{AB,r} \quad F_{AB,\phi} \quad F_{AB,\psi} \rfloor\\ &\quad = \lfloor F_{AB,x} \quad F_{AB,y} \quad F_{AB,z} \rfloor R_3(\phi)R_2(-\psi)\end{aligned} \tag{35}$$

Hence with all of the products of rotation matrices, which are functions of the sines and cosines of the Euler angles and the curvilinear coordinate angles, the resulting force expressions on the right-hand side of Eq. (35) are quite complicated, nonlinear expressions. Similarly, Eqs. (28–31) involve complicated, nonlinear expressions. On the left-hand sides, the angular velocity components are replaced with expressions involving the Euler angles, as defined in Table 1, and the angular acceleration components are replaced with the corresponding derivatives. The resulting expressions for the left-hand sides of Eqs. (28–31) are lengthy, nonlinear expressions. Note that similar expressions exist for spacecraft B, where β_1, β_2, and β_3 are simply substituted in place of α_1, α_2, and α_3. On the right-hand sides of Eqs. (28–30), the torques are expressed as components resolved on the body-fixed frame. Hence the magnetic moments must be transformed from the body-fixed to the global frame using Eq. (20), and the resulting torques, calculated using Eq. (26), must then be transformed from the global frame back to the body-fixed frame using Eq. (6):

$$\begin{aligned}\boldsymbol{T}_{AB} &= \lfloor T_{AB,x} \quad T_{AB,y} \quad T_{AB,z} \rfloor \hat{e}_G\\ &= \lfloor T_{AB,x} \quad T_{AB,y} \quad T_{AB,z} \rfloor R_3(\alpha_3)R_2(\alpha_2)R_1(\alpha_1)\hat{e}_A\end{aligned} \tag{36}$$

$$\begin{aligned}&\Rightarrow \lfloor T_{AB,1} \quad T_{AB,2} \quad T_{AB,3} \rfloor\\ &\quad = \lfloor T_{AB,x} \quad T_{AB,y} \quad T_{AB,z} \rfloor R_3(\alpha_3)R_2(\alpha_2)R_1(\alpha_1)\end{aligned} \tag{37}$$

The result, again, is several products of nonlinear terms in the Euler angles. Note that similar transformations must be made for the torques on spacecraft B:

$$\begin{aligned}&\lfloor T_{BA,1} \quad T_{BA,2} \quad T_{BA,3} \rfloor\\ &\quad = \lfloor T_{BA,x} \quad T_{BA,y} \quad T_{BA,z} \rfloor R_3(\beta_3)R_2(\beta_2)R_1(\beta_1)\end{aligned} \tag{38}$$

B. Linearized Equations of Motion

1. *Nominal Trajectory*

As explained in the preceding section, the nominal trajectory for the two-spacecraft EMFF array will be a steady-state spin maneuver of the two vehicles about the array center. While spinning, the vehicles should maintain a nominal separation distance, $2r_0$, remain within the global $\hat{e}_x$, $\hat{e}_y$ plane, and spin at a steady rate, $\dot{\phi}_0$, about their array center. Hence ψ is nominally zero, and the $\hat{e}_r$, $\hat{e}_\phi$ plane nominally coincides with the $\hat{e}_x$, $\hat{e}_y$ plane. Further, the nominal attitude of each spacecraft is such that $\hat{e}_A$ and $\hat{e}_B$ remain aligned with $\hat{e}_S$, and thus that the EMs aligned with $\hat{a}_1$ and $\hat{b}_1$ on spacecraft A and B, respectively, point toward the center of the array and align with each other. For this to occur, spacecraft A and B must rotate about the $\hat{a}_3$- and $\hat{b}_3$-axes, respectively, by the same angle, ϕ, that the array rotates about its center point. Further, $\hat{a}_3$ and $\hat{b}_3$ must remain aligned with the global $\hat{e}_z$-axis and thus remain perpendicular to the $\hat{e}_x$, $\hat{e}_y$ plane of rotation. This implies that the remaining Euler angles (α_1, α_2, β_1, and β_2) are nominally zero. With this description of the nominal trajectory, we write the nominal degree-of-freedom matrix, $\tilde{\boldsymbol{x}}_0$, as

$$\begin{aligned}\tilde{\boldsymbol{x}}_0 &= \lfloor r \quad \phi \quad \psi \quad \alpha_1 \quad \alpha_2 \quad \alpha_3 \quad \beta_1 \quad \beta_2 \quad \beta_3 \rfloor_0^T\\ &= \lfloor r_0 \quad \dot{\phi}_0 t \quad 0 \quad 0 \quad 0 \quad \dot{\phi}_0 t \quad 0 \quad 0 \quad \dot{\phi}_0 t \rfloor^T\end{aligned} \tag{39}$$

where subscripts "0" indicate nominal values. The nominal time-derivatives of the degrees of freedom are

$$\begin{aligned}\dot{\tilde{\boldsymbol{x}}}_0 &= \lfloor \dot{r} \quad \dot{\phi} \quad \dot{\psi} \quad \dot{\alpha}_1 \quad \dot{\alpha}_2 \quad \dot{\alpha}_3 \quad \dot{\beta}_1 \quad \dot{\beta}_2 \quad \dot{\beta}_3 \rfloor_0^T\\ &= \lfloor 0 \quad \dot{\phi}_0 \quad 0 \quad 0 \quad 0 \quad \dot{\phi}_0 \quad 0 \quad 0 \quad \dot{\phi}_0 \rfloor^T\end{aligned} \tag{40}$$

The nominal values $\delta_{3,0}$, $\varepsilon_{3,0}$, $\dot{\delta}_{3,0}$, and $\dot{\varepsilon}_{3,0}$ will be discussed at the end of this section. Equations (39) and (40) define the *nominal array trajectory*, so that displacements or rotations *relative to these nominal values* correspond to perturbed motion. Hence the degree-of-freedom matrix $\tilde{\boldsymbol{x}}$ and its derivative $\dot{\tilde{\boldsymbol{x}}}$ may be expressed as nominal values, plus perturbations from the nominal values:

$$\tilde{\boldsymbol{x}} = \boldsymbol{x}_0 + \Delta\tilde{\boldsymbol{x}}, \qquad \dot{\tilde{\boldsymbol{x}}} = \dot{\tilde{\boldsymbol{x}}}_0 + \Delta\dot{\tilde{\boldsymbol{x}}} \tag{41}$$

where the perturbations are

$$\Delta\tilde{\boldsymbol{x}} = \lfloor \Delta r \quad \Delta\phi \quad \Delta\psi \quad \Delta\alpha_1 \quad \Delta\alpha_2 \quad \Delta\alpha_3 \quad \Delta\beta_1 \quad \Delta\beta_2 \quad \Delta\beta_3 \rfloor^T \tag{42}$$

$$\Delta\dot{\tilde{\boldsymbol{x}}} = \lfloor\, \Delta\dot{r} \quad \Delta\dot{\phi} \quad \Delta\dot{\psi} \quad \Delta\dot{\alpha}_1 \quad \Delta\dot{\alpha}_2 \quad \Delta\dot{\alpha}_3 \quad \Delta\dot{\beta}_1 \quad \Delta\dot{\beta}_2 \quad \Delta\dot{\beta}_3 \,\rfloor^T \tag{43}$$

2. Nominal Control

The nominal control values are the magnetic moments and reaction wheel torques that would be required to maintain the nominal trajectory in a disturbance-free environment. Substituting the nominal trajectory, Eqs. (39) and (40) into the nonlinear equations of motion yields

$$(m_A + m_D)(-r_0\dot{\phi}_0^2) = F_{AB,r,0}, \qquad 0 = F_{AB,\phi,0}, \qquad 0 = F_{AB,\psi,0} \tag{44}$$

$$0 = T_{AB,1,0} - T_{Am_1,0}, \qquad 0 = T_{AB,2,0} - T_{Am_2,0}, \qquad 0 = T_{AB,3,0} - T_{Am_3,0}, \qquad 0 = T_{Am_3,0} \tag{45}$$

From Eqs. (44) and (45), we conclude that all RW motor torques are nominally zero, and all EM forces and torques are nominally zero, with the exception of the radial force component, $F_{AB,r}$. The nominal value, $F_{AB,r,0}$, of the radial force is calculated by creating the full nonlinear expression for the radial force and substituting the nominal values $\tilde{\boldsymbol{x}}_0$ and $\dot{\tilde{\boldsymbol{x}}}_0$ into the resulting expression. First we define nominal values for the magnetic moments:

$$\boldsymbol{\mu}_{A_i,0} = \mu_{A_i,0}\hat{a}_i, \qquad \boldsymbol{\mu}_{B_i,0} = \mu_{B_i,0}\hat{b}_i, \qquad i = 1, 2, 3 \tag{46}$$

so that the nominal value of the radial force is

$$F_{AB,r,0} = -\frac{3\mu_0\mu_{A_1,0}\mu_{B_1,0}}{32\pi r_0^4} \tag{47}$$

Substituting Eq. (47) into Eq. (44) yields

$$(m_A + m_D)r_0\dot{\phi}_0^2 = \frac{3\mu_0\mu_{A_1,0}\mu_{B_1,0}}{32\pi r_0^4} \tag{48}$$

Assuming the EMs oriented along $\hat{a}_1$ and $\hat{b}_1$, respectively, have equal nominal strengths, we find

$$\boldsymbol{\mu}_{A_1,0} = \boldsymbol{\mu}_{B_1,0} = \sqrt{(m_A + m_D)\frac{32\pi r_0^5\dot{\phi}_0^2}{3\mu_0}} \tag{49}$$

The right-hand side of Eq. (48) represents the control applied in the steady state, or the attractive force exerted on each spacecraft when the array dynamics and controls are nominal. The left-hand side represents the centripetal load that maintains each spacecraft in a steady-state spin maneuver. Equation (48) is a nominal force-balance equation, indicating that the attractive EM force provides the steady-state centripetal load of the spinning system. With this result, and the fact that the remaining EM force and torque components are zero, we find

$$\boldsymbol{\mu}_{A_i,0} = \boldsymbol{\mu}_{B_i,0} = 0, \qquad i = 2, 3 \tag{50}$$

Hence when the array is following its nominal trajectory without any disturbances, the EMs oriented along $\hat{a}_2$, $\hat{a}_3$, $\hat{b}_2$, and $\hat{b}_3$ are nominally unpowered. Similar to the matrix of degrees of freedom, we now define a column matrix of control values, $\boldsymbol{u}$, that are defined as nominal values, $\boldsymbol{u}_0$, plus perturbations, $\Delta\boldsymbol{u}$:

$$\boldsymbol{u} = \boldsymbol{u}_0 + \Delta\boldsymbol{u} \tag{51}$$

where

$$\boldsymbol{u} = \lfloor\, \mu_{A_1} \quad \mu_{A_2} \quad \mu_{A_3} \quad \mu_{B_1} \quad \mu_{B_2} \quad \mu_{B_3} \quad T_{Am_1} \quad T_{Am_2} \quad T_{Am_3} \quad T_{Bm_1} \quad T_{Bm_2} \quad T_{Bm_3} \,\rfloor^T \tag{52}$$

$$\Delta\boldsymbol{u} = \lfloor\, \Delta\mu_{A_1} \quad \Delta\mu_{A_2} \quad \Delta\mu_{A_3} \quad \Delta\mu_{B_1} \quad \Delta\mu_{B_2} \quad \Delta\mu_{B_3} \quad \Delta T_{Am_1} \quad \Delta T_{Am_2} \quad \Delta T_{Am_3} \quad \Delta T_{Bm_1} \quad \Delta T_{Bm_2} \quad \Delta T_{Bm_3} \,\rfloor^T \tag{53}$$

$$\begin{aligned}\boldsymbol{u}_0 &= \lfloor\, \mu_{A_1} \quad \mu_{A_2} \quad \mu_{A_3} \quad \mu_{B_1} \quad \mu_{B_2} \quad \mu_{B_3} \quad T_{Am_1} \quad T_{Am_2} \quad T_{Am_3} \quad T_{Bm_1} \quad T_{Bm_2} \quad T_{Bm_3} \,\rfloor_0^T \\ &= \lfloor\, \mu_{A_1,0} \quad 0 \quad 0 \quad \mu_{A_1,0} \quad 0 \quad 0 \quad 0 \quad 0 \quad 0 \quad 0 \quad 0 \quad 0 \,\rfloor^T\end{aligned} \tag{54}$$

3. Conservation of Angular Momentum

We now define $\delta_{3,0}$, $\varepsilon_{3,0}$, $\dot{\delta}_{3,0}$, and $\dot{\varepsilon}_{3,0}$ using the principle of conservation of angular momentum. Recall that RW-3 nominally stores the angular momentum of the spinning array. Hence for the nominal trajectory, the array spins at a constant rate, $\dot{\phi}_0$, and RW-3 spins at a constant rate to store the array's constant angular momentum. The sum of these momenta is thus constant, and if the RWs are at rest when the array is at rest, the sum is zero. Nominally the two spacecraft assume a circular trajectory in the global $\hat{e}_x$, $\hat{e}_y$ plane ($\psi = 0$), so that the conservation of angular momentum is expressed as

$$I_3^D(\dot{\delta}_{3,0} + \dot{\phi}_0) + [I_3^A + (m_A + m_D)r_0^2]\dot{\phi}_0 = 0 \tag{55}$$

The steady-state spin rate of RW-3 on spacecraft A is then

$$\dot{\delta}_{3,0} = -\dot{\phi}_0 \frac{(I_3^A + I_3^D) + (m_A + m_D) r_0^2}{I_3^D} \tag{56}$$

Notice that in order for Eq. (55) to be satisfied, $\dot{\phi}_0$ and $\dot{\delta}_{3,0}$ must be opposite in sign; in other words, if the array is spinning counterclockwise such that $\dot{\phi}_0 > 0$, the RW will spin clockwise such that $\dot{\delta}_{3,0} < 0$. Also, because we are assuming that spacecraft A and B are identical in mass and geometric properties, we can assume that their RWs nominally store equal amounts of the array's angular momentum, so that

$$\dot{\varepsilon}_{3,0} = \dot{\delta}_{3,0} \tag{57}$$

4. Linearization of Equations

Here we present the linearized equations of motion for the system, formulated by assuming that all motions are small relative to the nominal trajectory. We substitute for each degree of freedom and its derivative a nominal value, plus a perturbation. Similarly, we substitute for each control variable a nominal value, plus a perturbation. Because a linearized set of equations will capture only first-order dynamics, all second-order and higher-order products of perturbations are set to zero. This is equivalent to taking a first-order Taylor series expansion of the dynamics about the nominal trajectory and control values. We make the assumption that the spacecraft and RW are axially symmetric ($I_1^A = I_2^A$ and $I_1^D = I_2^D$), and with the assumption that spacecraft A and B are identical in mass and geometric properties, we arrive at the linearized equations of motion, written in second-order matrix form:

$$M\Delta\ddot{\tilde{\boldsymbol{x}}} + C\Delta\dot{\tilde{\boldsymbol{x}}} + K\Delta\tilde{\boldsymbol{x}} = F\Delta\boldsymbol{u} \tag{58}$$

where $\Delta\tilde{\boldsymbol{x}}$ and $\Delta\boldsymbol{u}$ are defined by Eqs. (42) and (53), respectively, and

$$M = \begin{bmatrix}
1 & 0 & 0 & 0 & 0 & 0 & 0 & 0 & 0 \\
0 & r_0 & 0 & 0 & 0 & 0 & 0 & 0 & 0 \\
0 & 0 & r_0 & 0 & 0 & 0 & 0 & 0 & 0 \\
0 & 0 & 0 & I_1^A + I_1^D & 0 & 0 & 0 & 0 & 0 \\
0 & 0 & 0 & 0 & I_1^A + I_1^D & 0 & 0 & 0 & 0 \\
0 & 0 & 0 & 0 & 0 & I_3^A & 0 & 0 & 0 \\
0 & 0 & 0 & 0 & 0 & 0 & I_1^A + I_1^D & 0 & 0 \\
0 & 0 & 0 & 0 & 0 & 0 & 0 & I_1^A + I_1^D & 0 \\
0 & 0 & 0 & 0 & 0 & 0 & 0 & 0 & I_3^A
\end{bmatrix} \tag{59}$$

$$C = \begin{bmatrix}
0 & -2r_0\dot{\phi}_0 & 0 & 0 & 0 & 0 & 0 & 0 & 0 \\
2\dot{\phi}_0 & 0 & 0 & 0 & 0 & 0 & 0 & 0 & 0 \\
0 & 0 & 0 & 0 & 0 & 0 & 0 & 0 & 0 \\
0 & 0 & 0 & 0 & -c_4 & 0 & 0 & 0 & 0 \\
0 & 0 & 0 & c_4 & 0 & 0 & 0 & 0 & 0 \\
0 & 0 & 0 & 0 & 0 & 0 & 0 & 0 & 0 \\
0 & 0 & 0 & 0 & 0 & 0 & 0 & -c_4 & 0 \\
0 & 0 & 0 & 0 & 0 & 0 & c_4 & 0 & 0 \\
0 & 0 & 0 & 0 & 0 & 0 & 0 & 0 & 0
\end{bmatrix} \tag{60}$$

$$K = \begin{bmatrix}
-5\dot{\phi}_0 & 0 & 0 & 0 & 0 & 0 & 0 & 0 & 0 \\
0 & -2c_1 & 0 & 0 & 0 & c_1 & 0 & 0 & c_1 \\
0 & 0 & -4c_1 & 0 & -c_1 & 0 & 0 & -c_1 & 0 \\
0 & 0 & 0 & -c_5 & 0 & 0 & 0 & 0 & 0 \\
0 & 0 & -3c_0 & 0 & -(c_5 + 2c_0) & 0 & 0 & -c_0 & 0 \\
0 & 3c_0 & 0 & 0 & 0 & -2c_0 & 0 & 0 & -c_0 \\
0 & 0 & 0 & 0 & 0 & 0 & -c_5 & 0 & 0 \\
0 & 0 & -3c_0 & 0 & -c_0 & 0 & 0 & -(c_5 + 2c_0) & 0 \\
0 & 3c_0 & 0 & 0 & 0 & -c_0 & 0 & 0 & -2c_0
\end{bmatrix} \tag{61}$$

$$F = \begin{bmatrix}
c_2 & 0 & 0 & c_2 & 0 & 0 & 0 & 0 & 0 & 0 & 0 & 0 \\
0 & -\frac{c_2}{2} & 0 & 0 & -\frac{c_2}{2} & 0 & 0 & 0 & 0 & 0 & 0 & 0 \\
0 & 0 & -\frac{c_2}{2} & 0 & 0 & -\frac{c_2}{2} & 0 & 0 & 0 & 0 & 0 & 0 \\
0 & 0 & 0 & 0 & 0 & 0 & -1 & 0 & 0 & 0 & 0 & 0 \\
0 & 0 & -2c_3 & 0 & 0 & -c_3 & 0 & -1 & 0 & 0 & 0 & 0 \\
0 & 2c_3 & 0 & 0 & c_3 & 0 & 0 & 0 & -1 & 0 & 0 & 0 \\
0 & 0 & 0 & 0 & 0 & 0 & 0 & 0 & 0 & -1 & 0 & 0 \\
0 & 0 & -c_3 & 0 & 0 & -2c_3 & 0 & 0 & 0 & 0 & -1 & 0 \\
0 & c_3 & 0 & 0 & 2c_3 & 0 & 0 & 0 & 0 & 0 & 0 & -1
\end{bmatrix} \tag{62}$$

$$c_0 \equiv \frac{-(m_A + m_D) r_0^2 \dot{\phi}_0^2}{3}, \qquad c_1 \equiv \frac{-r_0^2 \dot{\phi}_0^2}{2}$$
$$c_2 \equiv -\dot{\phi}_0 \sqrt{\frac{3\mu_0}{32\pi(m_A + m_D) r_0^3}} \tag{63}$$

$$c_3 \equiv \frac{(m_A + m_D) r_0}{3} c_2 = -\dot{\phi}_0 \sqrt{\frac{\mu_0 (m_A + m_D)}{96\pi r_0}} \tag{64}$$

$$c_4 = (2(I_1^A + I_1^D) + (m_A + m_D) r_0^2) \dot{\phi}_0,$$
$$c_5 = (I_1^A + I_1^D + (m_A + m_D) r_0^2) \dot{\phi}_0 \tag{65}$$

Notice that the damping matrix, C, contains skew-symmetric terms, $\pm c_4$. These terms represent the gyrostiffening effect of the spinning RWs on the spacecraft dynamics. Equation (58) may be expressed in first-order form:

$$\Delta \dot{\boldsymbol{x}} = A \Delta \boldsymbol{x} + B \Delta \boldsymbol{u} \tag{66}$$

where

$$A = \begin{bmatrix} 0 & I \\ -M^{-1}K & -M^{-1}C \end{bmatrix} \tag{67}$$

$$B = \begin{bmatrix} 0 \\ -M^{-1}F \end{bmatrix} \tag{68}$$

$$\Delta \boldsymbol{x} = \begin{Bmatrix} \Delta \tilde{\boldsymbol{x}} \\ \Delta \dot{\tilde{\boldsymbol{x}}} \end{Bmatrix} \tag{69}$$

I represents an $\frac{n}{2} \times \frac{n}{2}$ identity matrix, where $\frac{n}{2} = 9$ is the number of independent degrees of freedom in the system. $\Delta \boldsymbol{x}$ represents the state of the system and is an $n \times 1$ column matrix. Notice that the states of the RWs ($\Delta\delta_3$ and $\Delta\varepsilon_3$) do not appear in Eqs. (58–65). This is due to the fact that the linearized equations for the state dynamics of the spacecraft are independent of the states of the RWs, although the reverse is not true. Hence we can express the RW dynamics as a separate set of equations that are dependent on the spacecraft states:

$$\begin{bmatrix} I_3^D & 0 \\ 0 & I_3^D \end{bmatrix} \begin{Bmatrix} \Delta\ddot{\delta}_3 \\ \Delta\ddot{\varepsilon}_3 \end{Bmatrix} + \begin{bmatrix} -3c_0' & 2c_0' & c_0' \\ -3c_0' & c_0' & 2c_0' \end{bmatrix} \begin{Bmatrix} \Delta\phi \\ \Delta\alpha_3 \\ \Delta\beta_3 \end{Bmatrix}$$
$$= \begin{bmatrix} -2c_3' & -c_3' & I_3' & 0 \\ -c_3' & -2c_3' & 0 & I_3' \end{bmatrix} \begin{Bmatrix} \Delta\mu_{A_2} \\ \Delta\mu_{B_2} \\ \Delta T_{Am_3} \\ \Delta T_{Bm_3} \end{Bmatrix} \tag{70}$$

where $c_0' \equiv c_0 I_3^D / I_3^A$, $c_3' \equiv c_3 I_3^D / I_3^A$, and $I_3' \equiv (I_3^A + I_3^D)/I_3^A$.

IV. Stability Analysis and Control Design

A. Stability of Open-Loop Dynamics

We now investigate the stability of the open-loop, linearized dynamics. The A matrix is formed using Eq. (67). Then the "eig" command in the Matlab Symbolic Toolbox yields the following eigenvalues for the linearized two-spacecraft dynamics:

$$\lambda_{1,2} = 0 \tag{71}$$

Table 2 Physical parameters used to plot the eigenvalues in Fig. 4

Parameter	Description	Assigned value
r_0	Nominal array radius (half of the separation distance)	7.5 m
m_A	Spacecraft mass	600 kg
m_D	Reaction wheel mass	8.9 kg
I_3^A	Spacecraft inertia about z-axis	10 kg · m^2
I_1^A	Spacecraft inertia about radial axis	7 kg · m^2
I_3^D	Reaction wheel inertia about z-axis	0.1 kg · m^2
I_1^D	Reaction wheel inertia about radial axis	0.08 kg · m^2
$\dot{\phi}_0$	Nominal array spin rate	1 rev/2 h

$$\lambda_{13,14} = \pm i r_0 \dot{\phi}_0 \sqrt{\frac{m}{3I_3^A}} \tag{72}$$

$$\lambda_{15,16} = \pm \dot{\phi}_0 \sqrt{\frac{-mr_0^2 + \sqrt{(mr_0^2 + 2I_3^A)^2 + (4I_3^A)^2}}{2I_3^A}} \tag{73}$$

$$\lambda_{17,18} = \pm i \dot{\phi}_0 \sqrt{\frac{mr_0^2 + \sqrt{(mr_0^2 + 2I_3^A)^2 + (4I_3^A)^2}}{2I_3^A}} \tag{74}$$

where $m = m_A + m_D$, and λ_3–λ_{12} are very lengthy expressions [2], omitted here for brevity.

To represent the dynamics of a physical system, we substitute sample values into the A matrix and calculate the corresponding numerical eigenvalues. We choose mass and geometric properties resembling NASA's forthcoming TPF mission. These values are listed in Table 2. The resulting numerical eigenvalues are shown in the pole-zero map in Fig. 4. One eigenvalue is strictly stable, one is strictly unstable, two lie at the origin, and the remainder are "neutrally stable," lying on the imaginary axis. Note that only one pole is strictly unstable. Hence if we can stabilize this mode, we will have a good chance of controlling the entire system. It is interesting to note that the 16 nonzero eigenvalues increase in magnitude as the spin rate of the array increases. Hence the unstable pole, λ_{15}, grows increasingly unstable with increased steady-spin rate of the array. Also, the open-loop unstable pole increases in frequency as the nominal separation distance is increased.

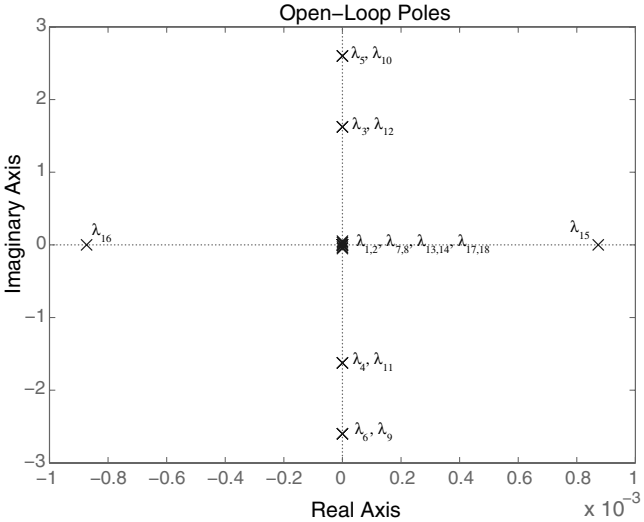

Fig. 4 Pole-zero map for two-spacecraft EMFF array, using geometric values in Table 2.

B. Controllability Analysis of Linearized Dynamics

To assess the controllability of the two-vehicle EMFF array, we form the controllability matrix [4]

$$C = [\,B \quad AB \quad A^2B \quad \cdots \quad A^{n-1}B\,] \tag{75}$$

From linear control theory, we know that the system is only controllable if $\text{rank}(C) = n$. Substituting A and B into Eq. (75), and testing the rank using the Matlab "rank" command yields

$$\text{rank (C)} = 18 = n \tag{76}$$

Hence all 18 states of the linearized system are controllable. Further, because even the unstable mode is controllable, the system is also stabilizable [4].

C. Linear Optimal Control Design

Because the system is controllable, we now design a controller. In control design, the simplest solution is often the best. Our system is highly nonlinear, both spatially in the electromagnetic forces and torques and dynamically from the rigid-body rotational dynamics of the bodies. The linearized set of equations is an idealized representation of the dynamics, accurate only for states and controls very close to the nominal values. However, if linear control can successfully stabilize and control this nonlinear, unstable system, it will greatly simplify the control design and implementation process compared to using nonlinear control techniques. For this reason, we attempt to apply linear control to this system, and we leave it as a future study to apply more sophisticated control techniques to improve the performance. We take a standard linear quadratic regulator (LQR) approach to the problem, which may be summarized as minimizing the following performance index [4]:

$$J = \int_0^\infty [\Delta \boldsymbol{x}^T(t) R_x \Delta \boldsymbol{x}(t) + \Delta \boldsymbol{u}^T(t) R_u \Delta \boldsymbol{u}(t)]\,\mathrm{d}t \tag{77}$$

where R_x is an $n \times n$ symmetric, positive semidefinite matrix of state penalties, R_u is a $p \times p$ symmetric, positive definite matrix of control penalties, and $p = 12$ is the number of control variables. The feedback control that minimizes Eq. (77) is

$$\Delta \boldsymbol{u} = -K \Delta \boldsymbol{x} \tag{78}$$

where the state gain matrix, K, is

$$K = -R_u^{-1} B^T P \tag{79}$$

and P is the solution of the matrix Riccati equation:

$$A^T P + PA - PBR_u^{-1}B^T P + R_x = 0 \tag{80}$$

Inserting the control in Eq. (78) into the linearized equations, Eq. (66), yields the *closed-loop linearized dynamics*:

$$\Delta \dot{\boldsymbol{x}} = A\Delta \boldsymbol{x} + B\Delta \boldsymbol{u} = A\Delta \boldsymbol{x} - BK\Delta \boldsymbol{x} = (A - BK)\Delta \boldsymbol{x} = A_{CL}\Delta \boldsymbol{x} \tag{81}$$

where $A_{CL} = A - BK$ is the closed-loop dynamic matrix.

The solution to Eqs. (77–80) is implemented using the Matlab Control Toolbox. The state penalty matrix, R_x, was chosen to be diagonal, with components as listed in Table 3. For the control penalty matrix, R_u, three different sets of penalties were chosen: "cheap" penalties in which actuators may be used liberally, "reasonable" penalties in which actuators are used in moderation, and "expensive" penalties in which actuators are used sparingly. The reasonable penalties are listed in Table 4. The cheap penalties are 100th of the reasonable penalties, and the expensive penalties are 100 times the reasonable penalties.

The state and control penalties in Tables 3 and 4, respectively, were selected through an iterative process. Initially, state penalties were chosen to emphasize the importance of the radial separation distance, followed by all other position and angle states and their derivatives. The rationale was to focus on the mode that is open-loop unstable (a radial divergence), and to thus penalize the radial separation distance most highly. The other state penalties were set relative to the radial separation penalty. The magnitudes were initially set arbitrarily (with the largest magnitudes near unity). For the control penalties, the magnetic moments were initially all assigned the same arbitrary penalty, and the torques were given another single penalty value much larger than the magnetic moment penalties (because the absolute values of their actuator signals would be much smaller). Both the state and control penalties were then iterated upon as follows: The closed-loop dynamics were formed, as described earlier, and then the closed-loop stability was investigated and the closed-loop dynamics were simulated, as described in the following sections. The *relative* values of the penalties were then tuned such that greater emphasis was placed on the degrees of freedom (and associated actuators) that were limiting the performance and stability behavior. The *absolute* values were scaled to yield realizable control magnitudes. Through this iterative process, the penalties were refined to yield those shown in Tables 3 and 4.

Table 3 State penalties for LQR control design

Degree of freedom (DOF)	Penalty	DOF derivative	Penalty
Δr	5	$\Delta \dot{r}$	10^{-2}
$\Delta \phi$	45	$\Delta \dot{\phi}$	5
$\Delta \psi$	45	$\Delta \dot{\psi}$	10^{-2}
$\Delta \alpha_1$	5	$\Delta \dot{\alpha}_1$	10^{-2}
$\Delta \alpha_2$	25	$\Delta \dot{\alpha}_2$	10^{-2}
$\Delta \alpha_3$	8	$\Delta \dot{\alpha}_3$	10^{-2}
$\Delta \beta_1$	5	$\Delta \dot{\beta}_1$	10^{-2}
$\Delta \beta_2$	25	$\Delta \dot{\beta}_2$	10^{-2}
$\Delta \beta_3$	8	$\Delta \dot{\beta}_3$	10^{-2}

Table 4 Actuator penalties for LQR control design

Magnetic moment	"Reasonable" penalty	RW torque	"Reasonable" penalty
$\Delta \mu_{A_1}$	10^{-10}	ΔT_{Am_1}	10^{-4}
$\Delta \mu_{A_2}$	10^{-12}	ΔT_{Am_2}	10^{-4}
$\Delta \mu_{A_3}$	10^{-12}	ΔT_{Am_3}	3
$\Delta \mu_{B_1}$	10^{-10}	ΔT_{Bm_1}	10^{-4}
$\Delta \mu_{B_2}$	10^{-12}	ΔT_{Bm_2}	10^{-4}
$\Delta \mu_{B_3}$	10^{-12}	ΔT_{Bm_3}	3

D. Stability of Closed-Loop Dynamics

Similar to the stability analysis of A, we now assess the stability of A_{CL} from Eq. (81) by solving for the closed-loop eigenvalues using the Matlab software. The closed-loop eigenvalues are shown in Fig. 5 for all three control levels described in the preceding section: cheap, reasonable, and expensive control. In all three cases, the closed-loop linearized dynamics are stable, because all closed-loop eigenvalues lie in the left-half complex plane. Although some eigenvalues lie much closer to the imaginary axis than others, they are all strictly stable.

V. Dynamics Simulations

In this section, we return to the nonlinear equations of motion, apply the linear control designed in the preceding section to form the closed-loop nonlinear dynamics, and then simulate these dynamics to demonstrate the effectiveness of the controller.

Two different methods are used to simulate the closed-loop dynamics, and both methods are implemented using the Matlab software. First, the nonlinear closed-loop dynamics are simulated using a differential equation simulation function, "ode15s." This is a built-in "stiff" solver in Matlab, useful for integrating differential equations with widely varying time constants. Because our closed-loop design model has poles of widely varying magnitude, as

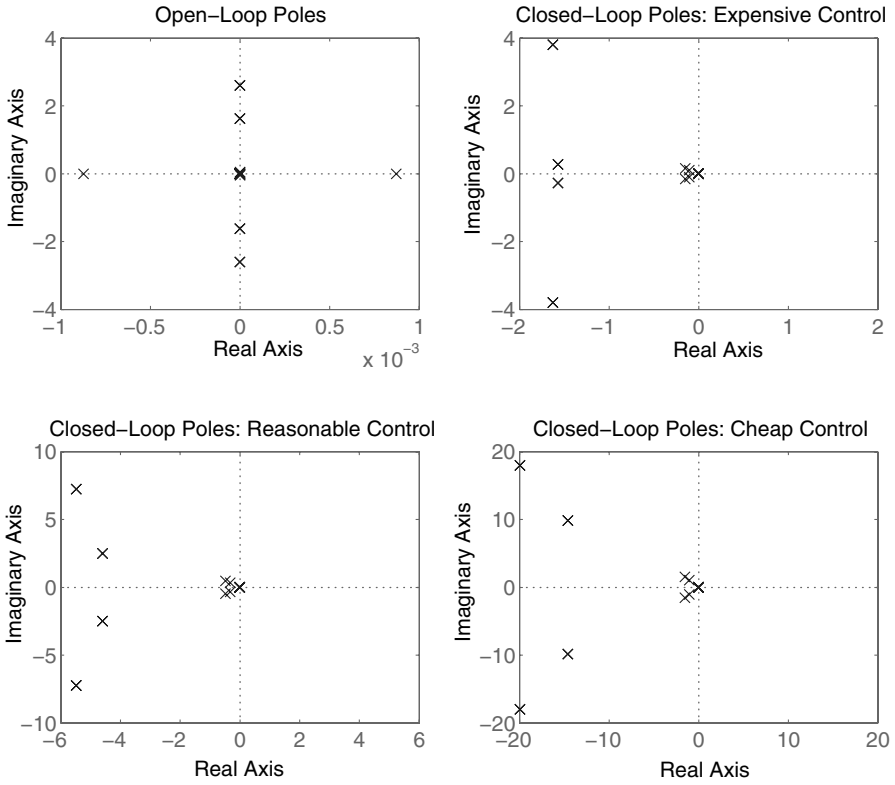

Fig. 5 Open-loop and closed-loop eigenvalues of the linearized design model.

depicted in Fig. 5, a stiff solver has proven more stable and accurate than nonstiff solvers.

In addition to simulating the closed-loop nonlinear equations, we also simulate the closed-loop linearized equations to assess the difference between the two sets of dynamics. We expect the two sets of equations to be similar in a regime close to the nominal trajectory, but this approximation becomes less accurate as the states and controls move away from their nominal values. To simulate the linearized equations, we use the Matlab "lsim" command, which is a function designed to integrate first-order differential equations in the form of Eq. (81).

To maintain a steady-state spin trajectory, our controller must provide the centripetal acceleration to each vehicle in the spinning array, using EMs to generate forces on the vehicles, and "reject" disturbances, or maintain the nominal trajectory in the presence of disturbances. One way to proceed would thus be to simulate the response to external disturbances. However, this would require that we first characterize the disturbances, and would yield a time response of the system that is dependent on this characterization. We instead simulate the free response of the system due to nonzero, nonnominal initial conditions. In this case, our primary concern is maintaining the nominal separation distance between the vehicles. From inspection of the system's eigenvectors [2], it is clear that the unstable mode of the open-loop dynamics involves a divergence of the radial separation distance from its nominal value. Hence to demonstrate the stability of the closed-loop system, it is useful to perturb the radial separation distance from its nominal value and witness the resulting free response. We focus here on the separation distance because of its role in the system stability; however, other "disturbances" may be simulated in a similar manner by applying nonzero initial conditions to the other degrees of freedom.

We first apply a 10% initial condition to the radial separation distance. Because linearized models generally represent their nonlinear counterparts accurately within $\sim$10% of the nominal trajectory, this initial condition should be large enough to demonstrate the differences between the nonlinear and linear simulations, as well as to test the success of the linear control on the fringe of the linear regime. The simulation results are shown in Fig. 6, where each degree of freedom of the system is plotted as a function of time. (Note that the deviations, $\Delta \boldsymbol{x}$, from the nominal values are plotted, as opposed to $\boldsymbol{x}$, the values themselves.) The radial separation distance is initially perturbed by 0.75 m, or 10% of the nominal 7.5 m separation radius, and the controller causes this variable to return to its nominal value. The simulations of the nonlinear and linearized dynamics differ slightly, but not significantly. Hence although the initial displacement is sizeable, large enough to test the limits of the linear model, the controller performs well, and the closed-loop dynamics remain stable. Figure 7 shows the time histories of the actuator signals used to control the system. The state and control penalties were chosen so that the magnitudes of the actuator signals would remain physically realistic. We see that this is indeed the case. From Eq. (19), we find that running 100 A of current through 600 turns of superconductive wire, with a coil radius of 0.75 m would yield a magnetic moment of $\sim$105 A $\cdot$ m^2. This is currently achievable with commercially available wire,[¶] but future state-of-the art wire will be even more enabling. As for the reaction wheel torques, low-mass reaction wheels have been demonstrated with motor torques on the order of 140 mN $\cdot$ m [5]. Hence our actuator signals are of reasonable magnitude. Note that although the states are plotted as deviations from nominal values, the controls are plotted as the actual magnitudes of the actuator signals, so that we may assess whether these values are physically realistic.

Figures 8 and 9 display the analogous state and actuator responses corresponding to an initial 35% (or $\sim$2.6 m) deviation of Δr. Despite the spatial nonlinearity of the electromagnetic actuators, the system remains stable, even at a very large displacement from the nominal trajectory. The dynamics of the nonlinear equations are now distinctly different from their idealized (linearized) counterparts, as expected.

Finally, Figs. 10 and 11 demonstrate that the system eventually becomes unstable when a 40% initial condition is placed on the separation radius. Contrary to intuition, the instability occurs in the rotational degrees of freedom, $\Delta\alpha_3$ and $\Delta\beta_3$, as opposed to in the radial separation variable, which we would expect to diverge. By

[¶]Data available online at "High Current Density Wire," http://www.amsuper.com [cited 2 February 2003].

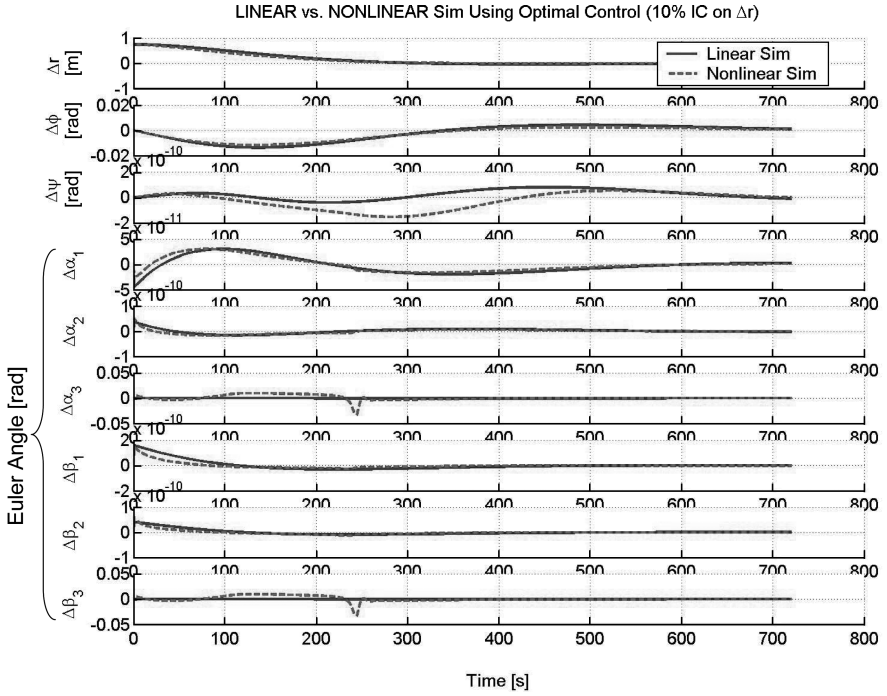

Fig. 6 Dynamic simulation with 10% initial condition on Δr: state response.

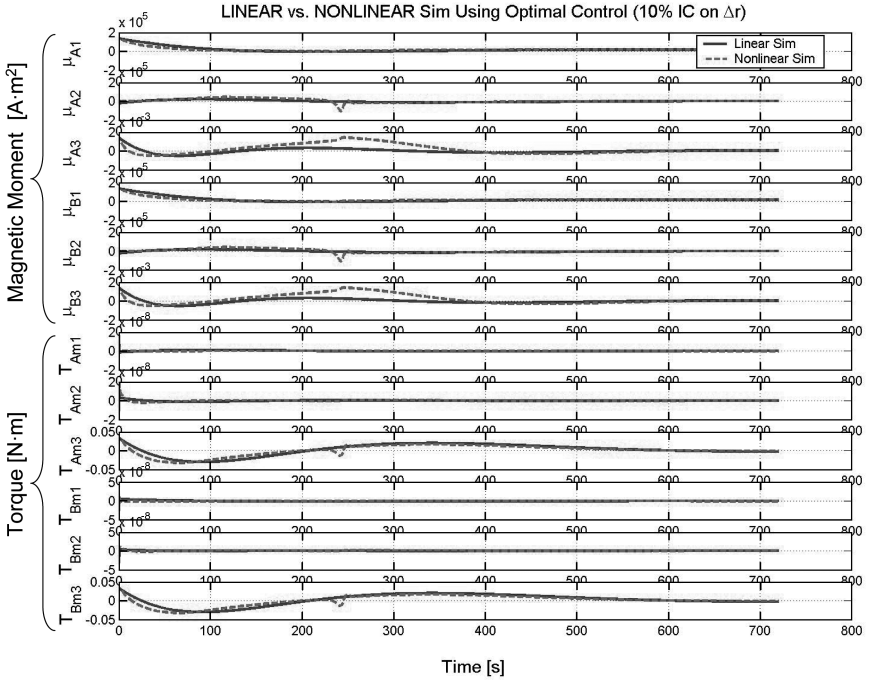

Fig. 7 Dynamic simulation with 10% initial condition on Δr: actuator response.

increasing the actuator capability of RW-3 on each spacecraft, we could increase the stability margin of this system and likely operate successfully, even with this 40% initial condition on Δr. Hence the limitation in this case is actually on the torque capability of the reaction wheel motors, as opposed to the strength of the electromagnetic actuators. This is very encouraging for the prospects of using electromagnets for relative control of formation flying arrays, because they do not seem to be the limiting factor on the stability of these systems.

VI. Applicability

Now that we have considered the dynamics and control of an electromagnetic formation flight system, we must also consider the applicability of the proposed electromagnetic actuators to various classes of missions. To generate large magnetic dipoles, a favorable electromagnetic coil design is one with many turns and high current. However, these properties must be traded against limitations on electromagnetic coil and solar array masses. Conventional coil conductors such as copper suffer from such high current application, because resistance causes significant heat generation and power losses. Therefore the design should use a coil that has the lowest resistance possible. Superconducting material has zero resistance when cooled below a critical temperature, thus eliminating thermal heating and power losses across the wire. There is a critical current density in the conductor above which the HTS will no longer conduct current at zero resistance. This clearly sets a limit on dipole strength. Furthermore, adding more coil will allow the dipole strength to be

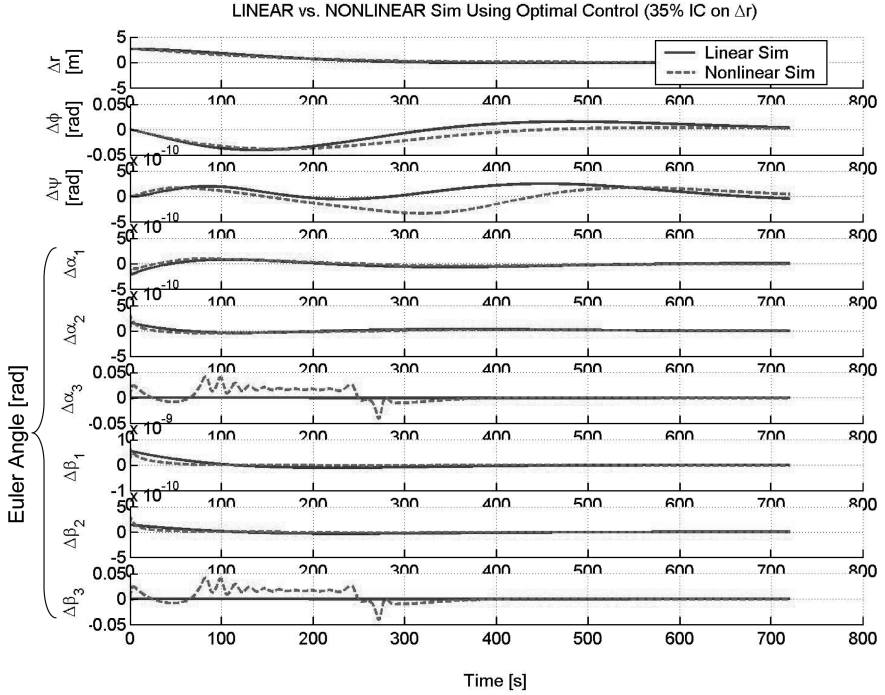

Fig. 8 Dynamic simulation with 35% initial condition on Δr: state response.

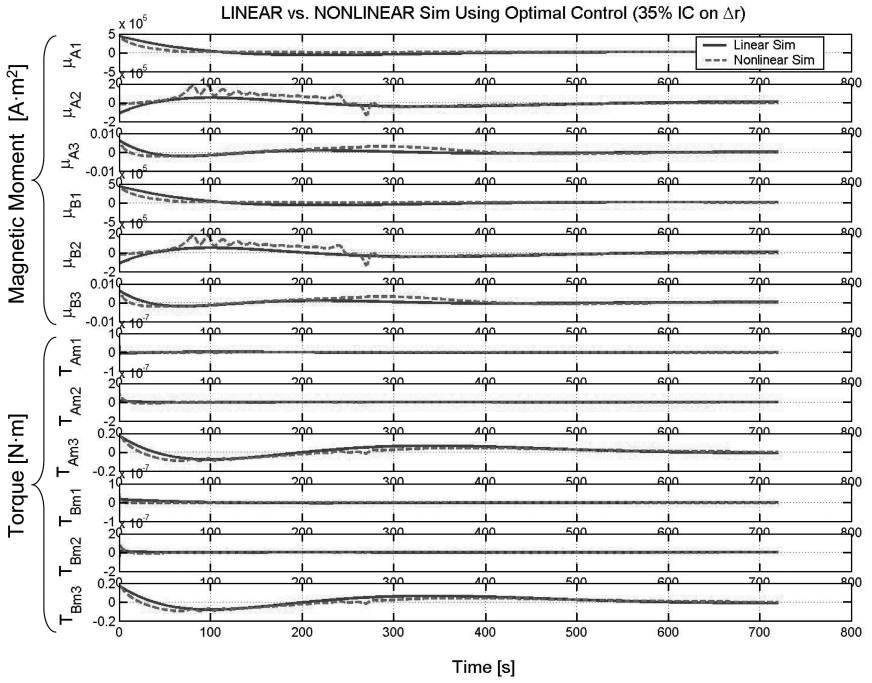

Fig. 9 Dynamic simulation with 35% initial condition on Δr: actuator response.

increased, but at the cost of mass. As a result, the current limit and the effect of high temperature superconductor (HTS) mass density can be modeled, respectively, as

$$i_{\max} = I_c A_c \qquad M_c = 2n\pi R_c A_c \rho_c \tag{82}$$

where I_c is the critical current density (A/m^2), A_c is the cross-sectional area of the HTS wire, M_c is the mass of the coil, R_c is the coil radius, and ρ_c is the volumetric mass density of the HTS wire. A simplified two-dimensional equation for the force between two identical vehicles with their dipoles aligned can be expressed by substituting Eqs. (19) and (82) into Eq. (25):

$$F_x = \frac{3}{8\pi}\mu_o\left(\frac{I_c}{\rho_c}\right)^2 M_{c_A} R_{c_A} M_{c_B} R_{c_B} \frac{1}{d^4} = \frac{3}{8\pi}\mu_o\left(\frac{I_c}{\rho_c}\right)^2 (M_c R_c)^2 \frac{1}{d^4} \tag{83}$$

Equation (83) illustrates the effect of separation distance on the coil requirements. There are three main design parameters in Eq. (83). The I_c/ρ_c quantity is the HTS technology parameter and is fixed for various types of HTS wire. With better HTS technology, either through higher current density or lower mass density wires, this technology factor can be improved. Current state-of-the-art high-strength HTS wire has a value of $I_c/\rho_c \sim 16,250$ A $\cdot$ m/kg at 77 K. The critical current density increases by a factor of 5 if the wire is maintained at 20 K. The quantity $M_c R_c$ is a coil design parameter that

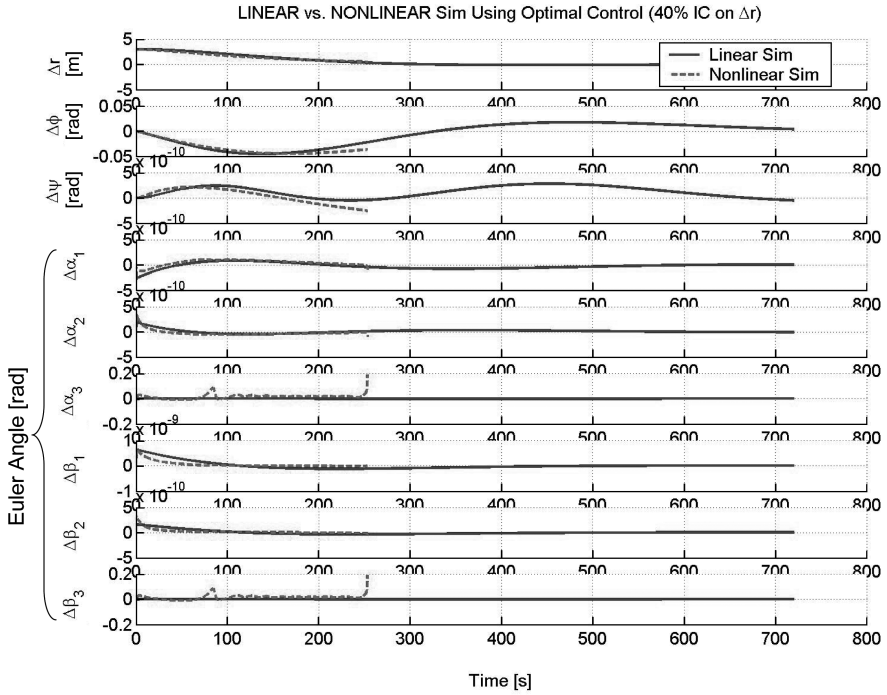

Fig. 10 Dynamic simulation with 40% initial condition on Δr: state response.

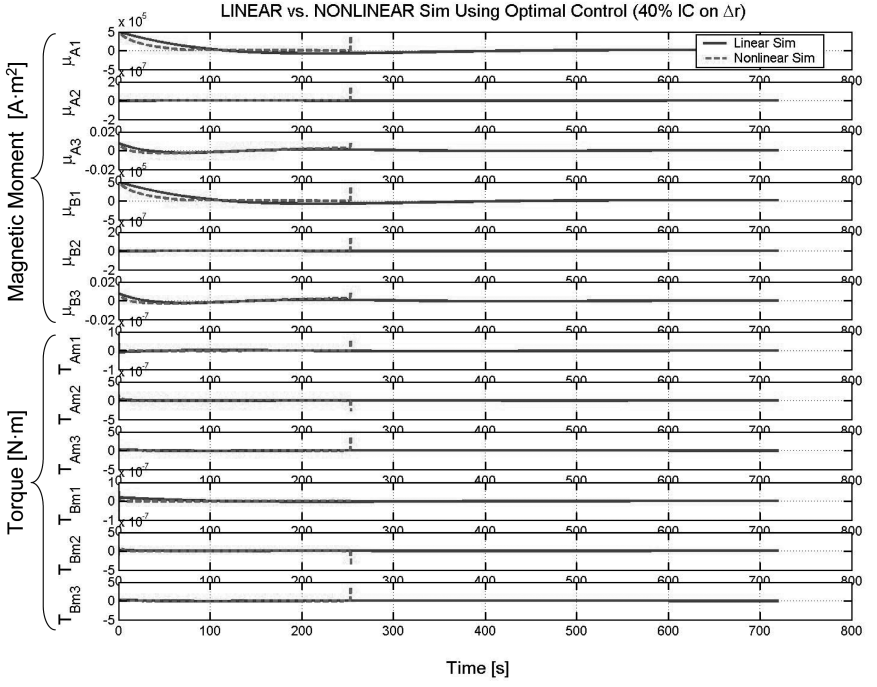

Fig. 11 Dynamic simulation with 40% initial condition on Δr: actuator response.

can vary according to the needs of the mission, because it is dependent on the number of turns of the coil and any constraints the spacecraft may have on the coil size. Finally, the array design parameter sets the separation distance, d. This is the design parameter most sensitive to changes because it has a fourth power relationship. Figure 12 [6] shows the axial force between two axially aligned dipoles as a function of their separation distance, for both state-of-the-art HTS technology (12a) and a factor of 3 improvement (12b) in I_c/ρ_c. Curves are shown for different coil designs ($M_c R_c$). For example, if two satellites with 1 m radius coils need 10 mN of thrust and 30 kg is dedicated to the coil on each satellite, this force can be achieved using state-of-the-art HTS at a separation of 43 m, indicated by the circle in Fig. 12a. This same force can be generated at a separation of approximately 77 m using an HTS technology with a three times improvement, indicated by the circle in Fig. 12b. Whereas these values are encouraging, they can be further improved with additional advances in HTS technology, or with additional mass and volume allocations for the coils. In this sense, EMFF appears to be a promising technology for 10–100 m class missions, and perhaps for even larger scale missions. The challenges of operating EMFF in low Earth orbit including the J_2 disturbance and the Earth's magnetic field have been addressed by Ahsun [7] and Schweighart [8].

VII. Conclusions

In this paper, we have introduced the nonlinear and linearized dynamics of a two-spacecraft EMFF system. We have shown the open-loop dynamics to be unstable but stabilizable using feedback

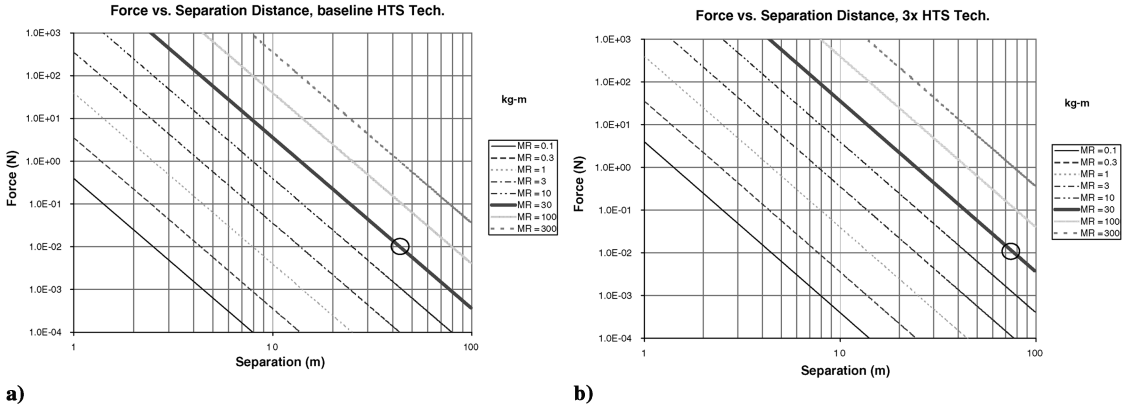

Fig. 12 Axial force vs separation distance for a) current HTS technology, and b) a factor of 3 improvement.

control. We have demonstrated that the system is controllable, designed a linear optimal controller, and simulated the closed-loop dynamics. The simulations indicate that linear optimal control has great potential to be applied to electromagnetic formation flying (EMFF) systems, even in regimes that are significantly different from the nominal trajectory. It was shown that the controller becomes impractical when a 40% deviation from initial conditions is placed on the separation radius. Further, the spatial nonlinearity of the electromagnetic actuators may not be the limiting factor in maintaining the closed-loop stability of spinning EMFF arrays. Hence EMFF is a potentially viable and physically realizable concept that may prove useful for stabilizing arrays, as well as for rejecting disturbances. In addition, because it eliminates the lifetime limitations and optical contamination issues associated with thrusters, EMFF may be a very promising technique for relative formation control.

References

[1] Kong, E. M. C., Kwon, D. W., Schweighart, S. A., Elias, L. M., Sedwick, R. J., and Miller, D. W., "Electromagnetic Formation Flight for Multisatellite Arrays," *Journal of Spacecraft and Rockets*, Vol. 41, No. 4, July–Aug. 2004, pp. 659–666.

[2] Elias, L. M., "Dynamics of Multi-Body Space Systems Including Reaction Wheel Gyrostiffening Effects: Structurally Connected and Electromagnetic Formation Flying Architectures," Ph.D. Thesis, Space System Laboratory, Rept. 5-04, Massachusetts Institute of Technology, Cambridge, MA, March 2004.

[3] Schwartz, M. S., *Principles of Electrodynamics*, Dover, New York, 1987.

[4] Belanger, P. R., *Control Engineering: A Modern Approach*, Oxford Univ. Press, New York, 1995.

[5] Ahronovich, E., and Balling, M., "Reaction Wheel and Drive Electronics for LeoStar Class Vehicles," SSC Paper 98-I-5, Aug.–Sept. 1998.

[6] Kwon, D., Miller, D. W., and Sedwick, R., "Electromagnetic Formation Flight for Sparse Aperture Arrays," Lockheed Martin Advanced Technology Center and NASA Jet Propulsion Laboratory, Paper 51, Sept. 2004.

[7] Ahsun, U., "Dynamics and Control of Electromagnetic Satellite Formations in Low Earth Orbits," AIAA Paper 2006-6590Aug. 2006.

[8] Schweighart, S. A., "Electromagnetic Formation Flight—Dipole Solution Planning," Ph.D. Thesis, Space Systems Laboratory, Rept. 9-05, Massachusetts Institute of Technology, Cambridge, MA, June 2005.